



Article

Nanoscale-Resistive Switching in Forming-Free Zinc Oxide Memristive Structures

Roman V. Tominov ¹, Zakhar E. Vakulov ², Nikita V. Polupanov ³, Aleksandr V. Saenko ¹, Vadim I. Avilov ⁴, Oleg A. Ageev ⁴ and Vladimir A. Smirnov ^{1,*}

- ¹ Department of Radioelectronics and Nanoelectronics, Institute of Nanotechnologies, Electronics and Electronic Equipment Engineering, Southern Federal University, 347922 Taganrog, Russia; tominov@sfedu.ru (R.V.T.); avsaenko@sfedu.ru (A.V.S.)
- ² Federal Research Centre the Southern Scientific Centre of the Russian Academy of Sciences, 344006 Rostov-on-Don, Russia; vakulov@ssc-ras.ru
- ³ Laboratory of Functional Nanomaterials Technology, Southern Federal University, 347922 Taganrog, Russia; npolupanov@sfedu.ru
- ⁴ Department of Micro- and Nanoelectronics, Institute of Nanotechnologies, Electronics and Electronic Equipment Engineering, Southern Federal University, 347922 Taganrog, Russia; avilovvi@sfedu.ru (V.I.A.); ageev@sfedu.ru (O.A.A.)
- * Correspondence: vasmirnov@sfedu.ru

Abstract: This article presents the results of experimental studies of the impact of electrode material and the effect of nanoscale film thickness on the resistive switching in forming-free nanocrystalline ZnO films grown by pulsed laser deposition. It was demonstrated that the nanocrystalline ZnO film with TiN, Pt, ZnO:In, and ZnO:Pd bottom electrodes exhibits a nonlinear bipolar effect of forming-free resistive switching. The sample with Pt showed the highest resistance values R_{HRS} and R_{LRS} and the highest value of $U_{set} = 2.7 \pm 0.4$ V. The samples with the ZnO:In and ZnO:Pd bottom electrode showed the lowest U_{set} and U_{res} values. An increase in the number of laser pulses from 1000 to 5000 was shown to lead to an increase in the thickness of the nanocrystalline ZnO film from 7.2 ± 2.5 nm to 53.6 ± 18.3 nm. The dependence of electrophysical parameters (electron concentration, electron mobility, and resistivity) on the thickness of the forming-free nanocrystalline ZnO film for the TiN/ZnO/W structure was investigated. The endurance test and homogeneity test for TiN/ZnO/W structures were performed. The structure $Al_2O_3/TiN/ZnO/W$ with a nanocrystalline ZnO thickness 41.2 ± 9.7 nm was shown to be preferable for the manufacture of ReRAM and memristive neuromorphic systems due to the highest value of $R_{HRS}/R_{LRS} = 2307.8 \pm 166.4$ and low values of $U_{set} = 1.9 \pm 0.2$ V and $U_{res} = -1.3 \pm 0.5$ V. It was demonstrated that the use of the TiN top electrode in the $Al_2O_3/TiN/ZnO$ memristor structure allowed for the reduction in U_{set} and U_{res} and the increase in the R_{HRS}/R_{LRS} ratio. The results obtained can be used in the manufacturing of resistive-switching nanoscale devices for neuromorphic computing based on the forming-free nanocrystalline ZnO oxide films.

Keywords: neuromorphic systems; memristor; ReRAM; resistive switching; forming-free nanocrystalline ZnO; pulsed laser deposition



Citation: Tominov, R.V.; Vakulov, Z.E.; Polupanov, N.V.; Saenko, A.V.; Avilov, V.I.; Ageev, O.A.; Smirnov, V.A. Nanoscale-Resistive Switching in Forming-Free Zinc Oxide Memristive Structures. *Nanomaterials* **2022**, *12*, 455. <https://doi.org/10.3390/nano12030455>

Academic Editor: Wan Sik Hwang

Received: 13 December 2021

Accepted: 25 January 2022

Published: 28 January 2022

Publisher's Note: MDPI stays neutral with regard to jurisdictional claims in published maps and institutional affiliations.



Copyright: © 2022 by the authors. Licensee MDPI, Basel, Switzerland. This article is an open access article distributed under the terms and conditions of the Creative Commons Attribution (CC BY) license (<https://creativecommons.org/licenses/by/4.0/>).

1. Introduction

Over the past few decades, the information-technology market has grown rapidly, largely because the performance of computing systems has improved significantly over time due to Moore's law [1–4]. Big-data processing is considered a new benchmark in addition to performance, which is of great importance in applications such as the Internet of Things (IoT), autonomous vehicles, and adaptive control and management systems [5,6]. Currently, further increases in the efficiency of big-data processing are limited by the resolution and the cost of manufacturing complementary metal oxide semiconductor (CMOS) transistors

less than 10 nanometers in size, creating the difficulty of sustainable and cost-effective scaling [7,8]. Therefore, there is a need to develop and research a new base of non-volatile elements of electronics with increased computational efficiency, which would meet the requirements of the information-technology market [9–13].

Memristor (ReRAM) is a memory and computing device that has appeared in the last few years and has shown great promise as a new-generation universal memory capable of operating in both digital and analog modes [14,15]. The advantages of ReRAM include non-volatility, low power consumption, high speed, small dimensions (~10 nm), as well as low manufacturing costs, and the ability to integrate with CMOS technology [16,17]. It should be noted that there is a theoretical possibility of reducing the ReRAM memory element to the atomic level, which will further improve the characteristics of the resistive switching effect by improving the uniformity of the nanoscale conduction channel, as well as reducing the current flowing through the ReRAM memory element, which will lead to a further decrease in power consumption [18–29].

The resistive switching effect is exhibited in many classes of materials, such as chalcogenides, perovskites, organic compounds, solid state electrolytes, graphene, and metal oxides [30–40]. Among the latter are binary oxides such as ZnO, HfO₂, ZrO₂, NiO, TiO₂, WO₃, TaO_x, and Gd₂O₃, which is of particular interest due to its compatibility with CMOS technology, multi-bit switching, and simple chemistry [41–48]. ZnO-based devices are used to simulate biological neurons and synaptic functions [49,50]. One of the main problems in the manufacture of ReRAM is obtaining controlled characteristics of switching behavior and electrical properties. From a semiconductor physics point of view, the metal/oxide interface and oxide thickness are key factors in determining the formation of oxygen vacancies and charge transport. Therefore, it is important to study the influence of geometric and electrophysical parameters, as well as the influence of the electrode material and their doping on the values and range of resistances of the high resistance state (R_{HRS}) and the low resistance state (R_{LRS}) for the manufacture of ReRAM elements of energy-efficient neuromorphic systems operating at low switching voltages (U_{set} and U_{res}) [51–57]. Despite several works reporting the observation of resistive switching in ZnO, there is still a lack of knowledge about various aspects for the manufacture of elements of memristive neuromorphic systems based on this material.

There are many metal-oxide film-fabrication methods: atomic layer deposition (ALD) [58,59], the sol-gel method [60], magnetron sputtering [61,62], and pulsed laser deposition (PLD) [63]. Forming-free nanocrystalline ZnO films grown using PLD have been shown to exhibit improved resistive switching characteristics, with higher R_{HRS}/R_{LRS} ratios and lower operating voltages [64–67]. PLD is a relatively inexpensive technology for growing thin films that meets the requirements for fabricating memristive devices, primarily because of the possibility of precise adjustment of the electrophysical parameters of the oxide by varying the growth parameters.

In this work, we experimentally investigated the influence of the bottom electrode (BE) material and the thickness of the forming-free nanocrystalline ZnO film on the resistances of the R_{HRS} , R_{LRS} , and R_{HRS}/R_{LRS} , as well as on the switching voltages U_{set} and U_{res} . Then, nanoscale resistive switching study of forming-free nanocrystalline ZnO films was represented using conductive atomic force microscopy (CAFM). The influence of PLD growth conditions on the electrophysical and morphological parameters of the obtained films was investigated. In the end, we fabricated and investigated forming-free resistive switching in Al₂O₃/TiN/ZnO/TiN memristive structures. We considered that the new results obtained in the article will be useful to readers and can be used in the development of neuromorphic systems based on memristor structures and zinc oxide.

2. Materials and Methods

To investigate the effect of the bottom-electrode material on resistive switching in the nanocrystalline ZnO film, samples with different bottom-electrode materials (TiN, Pt, ZnO:In, ZnO:Pd) were prepared using a Pioneer 180 PLD module (Neocera LCC,

Beltsville, MD, USA) with a KrF excimer laser ($\lambda = 248$ nm). Sapphire wafer (Al_2O_3) was used as a substrate. An high-energy electron-diffraction system (k-Space Associates Inc., Dexter, MI, USA) entering the composition of the PLD module was used for RHEED study. The lattice constant was determined using the kSA-400 (Version 1.0) software. The bottom electrodes were grown under the following conditions: substrate temperature: 500 °C; target–wafer distance: 50 mm; background pressure (vacuum): 10^{-5} Torr; pulse energy: 400 mJ; laser-pulse repetition rate: 10 Hz; and number of laser pulses: 10,000. Then, on the bottom electrodes of all samples in a single vacuum cycle, a nanocrystalline ZnO film was deposited on the PLD under the following conditions: substrate temperature: 450 °C; target–substrate distance: 60 mm; oxygen pressure: 0.5 mTorr; pulse energy: 400 mJ; laser-pulse repetition rate: 10 Hz; number of laser pulses: 3000. All nanocrystalline ZnO films were annealed in a nitrogen atmosphere with a pressure of 10^{-3} Torr at a temperature of 1200 °C for 10 h for forming free resistive switching [64].

For electrical measurements, the nanocrystalline ZnO films were deposited through a special mask pattern to provide access to the bottom electrode. Thus, the film was not deposited around the bottom electrode protected by the mask.

The structure of ZnO films was studied by X-ray diffractometry (XRD) using a Rigaku Miniflex 600 diffractometer (Rigaku Corporation, Tokyo, Japan).

The temperature dependences of the change in Gibbs free energy (Ellingham diagram) were calculated using the FactSage 6.2 software package for chemical-reaction analysis (GTT-Technologies, Herzogenrath, Germany) with an updated electronic database of the temperature dependence of thermophysical parameters.

To study the nanoscale-resistive switching in forming-free ZnO films, we used a conductive atomic force microscopy (CAFM) mode on the Ntegra Probe Nanolaboratory (NT-MDT, Zelenograd, Russia). For this aim, the method described in [64,65] was used. As a result, CAFM images of the zinc oxide resistive switching were obtained under the following regimes: HRS spot at +5 V, LRS spot at −5 V, and CAFM reading voltage +1 V. Spots were investigated during 10^4 s. Based on the results obtained, the retention test was plotted.

Electric measurements were carried out using a semiconductor characterization system Keithley 4200-SCS (Keithley Instruments, Solon, OH, USA) and an EM-6070A submicrometer probe system (Planar, Minsk, Belarus) with 100 nm tip diameter tungsten (W) probes. The bottom electrode was grounded for all samples. To prevent thermal breakdown of the nanocrystalline ZnO film, a compliance current of 10^{-4} A was set during the electric measurements. As a result, the current-voltage curves (CVC) were obtained at a voltage sweep of −3 to +3 for 10 cycles for each sample at the same point on the ZnO surface. The read voltage was 0.5 V. Curve analysis was implemented using Origin 8.1 software (OriginLab Corporation, Northampton, MA, USA). Based on the results obtained, the resistances R_{HRS} , R_{LRS} , R_{HRS}/R_{LRS} , U_{set} , and U_{res} were evaluated.

The thickness of the nanocrystalline ZnO film was investigated by measuring the height of the TiN/ZnO “step” made by photolithography. For this, $\text{Al}_2\text{O}_3/\text{TiN}/\text{ZnO}$ samples were prepared with different numbers of laser pulses for ZnO from 1000 to 5000. Then, the FP-383 photoresist was applied to the ZnO film by the centrifugation method at a rotation speed of 4000 rpm. The photoresist film was exposed through a photomask to UV radiation for 2 min, developed in a 5% aqueous solution of KOH, and tanned at 110 °C for 20 min. Areas of the ZnO film that were not protected by photoresist were etched in an ammonium hydroxide/water solution (1:2) for 30 s. Photoresist residues were removed with dimethylformamide. The step height (Figure S1) and the surface roughness were investigated using the Ntegra Probe Nanolaboratory in semi-contact AFM mode using NSG11 cantilevers. AFM scanning was carried out with the following parameters: velocity: 80 $\mu\text{m}/\text{s}$; scan area: $1 \times 1 \mu\text{m}^2$; and SetPoint: 7 nA. AFM image processing was performed using Image Analysis software. To confirm the AFM results, we also investigated the nanocrystalline ZnO film surface using a Nova NanoLab 600 scanning electron microscope (FEI Company, Hillsboro, OR, USA). SEM images were obtained with

the following parameters: acceleration voltage: 10 kV and magnification: 300,000 \times . Based on the experimental results obtained, the dependence of the nanocrystalline ZnO film thickness and surface roughness on the number of laser pulses were tabled.

The electrophysical parameters of the nanocrystalline ZnO films were studied using an Ecopia HMS-3000 Hall effect system (Ecopia Co., Anyang, Korea). The dependences of the electron concentration, electron mobility, and resistivity of the nanocrystalline ZnO films on their thicknesses were plotted. The study of the influence of the thickness of the nanocrystalline ZnO film on resistive switching in the Al₂O₃/TiN/ZnO structure was also carried out with the Keithley 4200-SCS semiconductor characterization system. For this purpose, the CVCs were measured at the same point on the ZnO surface at voltage sweeps of -3 to $+3$ for each sample. The read voltage was 0.5 V. Based on the obtained results, the R_{HRS} , R_{LRS} , and R_{HRS}/R_{LRS} dependences of the Al₂O₃/TiN/ZnO structures on the thickness of the forming-free nanocrystalline ZnO film were plotted. Furthermore, the dependence of R_{HRSp} , R_{LRSp} , and R_{HRSp}/R_{LRSp} on the switching cycle number (endurance test) was plotted. To study the effect of resistive switching at different points on the ZnO surface (homogeneity test), CVCs were obtained at different points on the surface of the forming-free nanocrystalline ZnO film on each sample. Based on the results obtained, R_{HRSs} , R_{LRSs} , and R_{HRSs}/R_{LRSs} at different points on the surface of the ZnO film of each sample were determined and tabled.

To study the influence of the top electrode on the effect of resistive switching, Al₂O₃/TiN/ZnO/TiN memristive structures (16 samples) were fabricated. The film of the top electrode was grown by PLD in regimes identical to those of the bottom electrode. The CVCs were also measured at voltage sweeps of -4 to $+4$ V for each sample. The read voltage was 0.5 V. Based on the results obtained, the endurance test and device-to-device reproducibility were plotted.

To study the influence of the amplitude pulse voltage (U_A) and the pulse time duration (t_A) on the R_{HRS}/R_{LRS} ratio, an endurance test was carried out in the range of 3 to 7 V and 20 to 60 ms for 1000 cycles for each of the U_A and t_A values, respectively. Based on the experimental results obtained, the dependences of the R_{HRS}/R_{LRS} ratio on U_A and t_A were plotted.

3. Results

Figure 1a–d shows the morphology of the zinc-oxide film. An increase in the number of laser pulses from 1000 to 5000 was shown to lead to an increase in surface roughness from 3.1 ± 0.7 nm to 19.8 ± 3.5 nm. The XRD spectrum of Al₂O₃/TiN/ZnO was characterized by a pronounced peak of ZnO (101) at 34° and ZnO (004) at 74° (Figure 1e). The lattice constant was established to be equal to 0.31 nm (Figure 1f). Thus, it was shown that the zinc-oxide film studied had a nanocrystalline structure.

An analysis of the results showed that a nanocrystalline ZnO film with a bottom electrode of TiN, Pt, and ZnO:In and ZnO:Pd exhibits non-linear bipolar forming-free resistive switching, according to which the electric field gradient and the kinetic energy of the electrons prevail over the concentration gradient and the temperature gradient [16] (Figure 2).

The values obtained for the R_{HRS} and R_{LRS} resistances, the R_{HRS}/R_{LRS} ratio, and the switching voltages U_{set} and U_{res} are shown in Table 1. It was shown that the highest ratio $R_{HRS}/R_{LRS} = 2307.8 \pm 166.4$ was possessed by a sample with a TiN bottom electrode. The sample with Pt shows high resistance, R_{HRS} and R_{LRS} values, and the highest value of $U_{set} = 2.7 \pm 0.4$ V. The samples with bottom electrodes made of ZnO:In and ZnO:Pd showed lower values of the R_{HRS} and R_{LRS} and the R_{HRS}/R_{LRS} ratio, compared to those of TiN and Pt, but were more stable than U_{set} and U_{res} . The sample with the ZnO:Pd bottom electrode, in this case, showed the lowest $U_{set} = 1.2 \pm 0.1$ V.

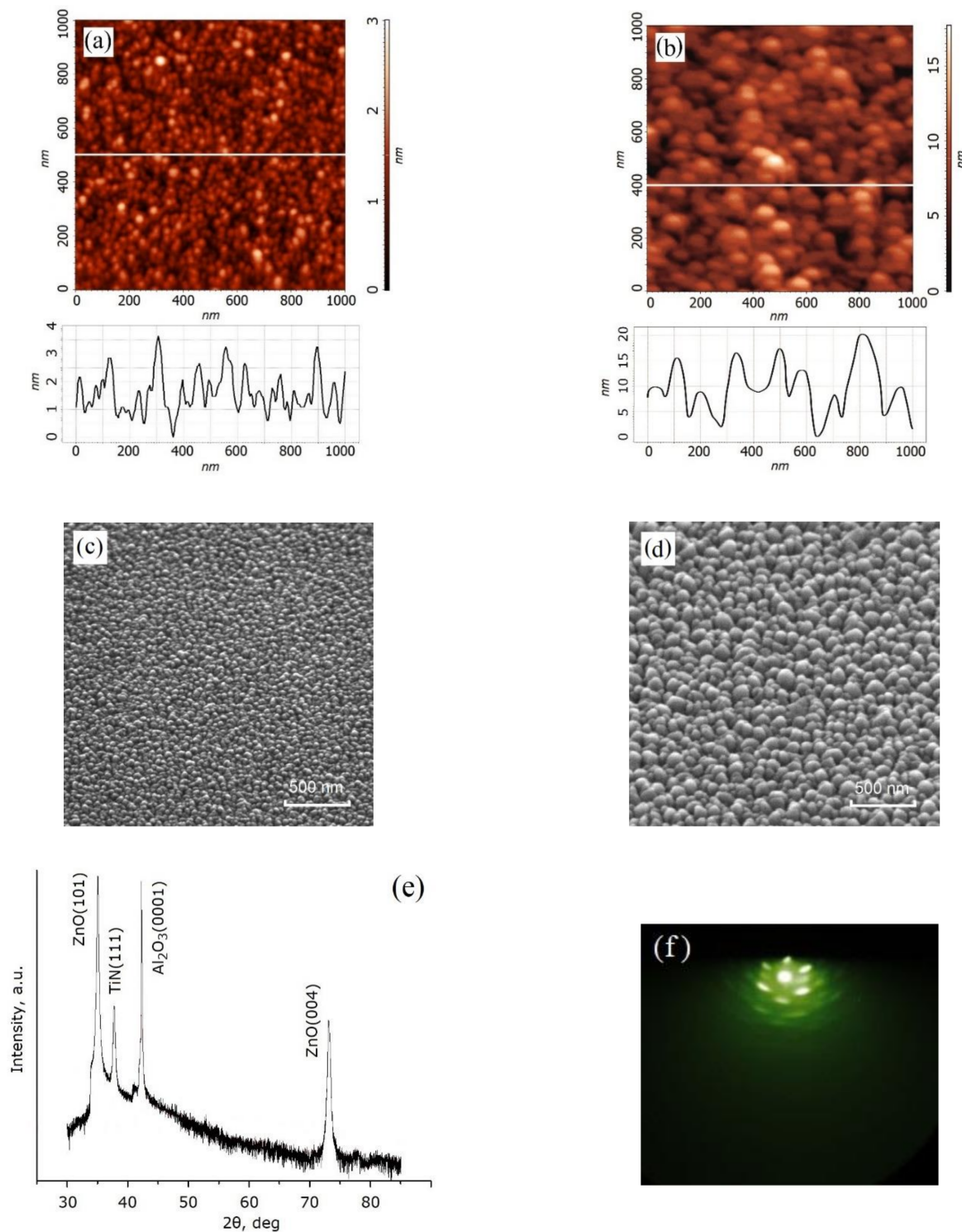


Figure 1. Nanocrystalline ZnO films surface at 1000 (a,c,e) and 5000 (b,d,f) number of laser pulses: (a,b)—AFM-image and AFM cross-section along the white line; (c,d)—SEM images; (e)—XRD spectrum of the $\text{Al}_2\text{O}_3/\text{TiN}/\text{ZnO}$ structure; (f)—RHEED pattern.

To explain the results obtained, an Ellingham diagram (Figure 3a) was built for the metal oxides formed due to the reduction reaction at the interface between the electrode and the forming-free nanocrystalline ZnO film (Equations (S1)–(S9)).

The interface between a metal electrode and an oxide is known to play a key role in resistive switching, especially for bipolar switching. The oxygen vacancies resulting

from the redox reaction determine the potential barrier at the metal/oxide interface [61,62]. Bipolar switching is common for asymmetric structures. Different materials of the top and bottom electrodes lead to the fact that the interface with many oxygen vacancies serves as a reservoir (the base of the nanoscale conduction channel); switching occurs at the opposite interface with a smaller number of oxygen vacancies (the apex of the nanoscale conduction channel). A rectifying contact is observed at interfaces with a small number of oxygen vacancies; an increase in the number of oxygen vacancies leads to ohmic conductivity. In turn, the number of oxygen vacancies is determined by the Gibbs free energy change (ΔG), an increase that leads to an increase in the number of oxygen vacancies, and a decrease that leads to a decrease in the number of oxygen vacancies.

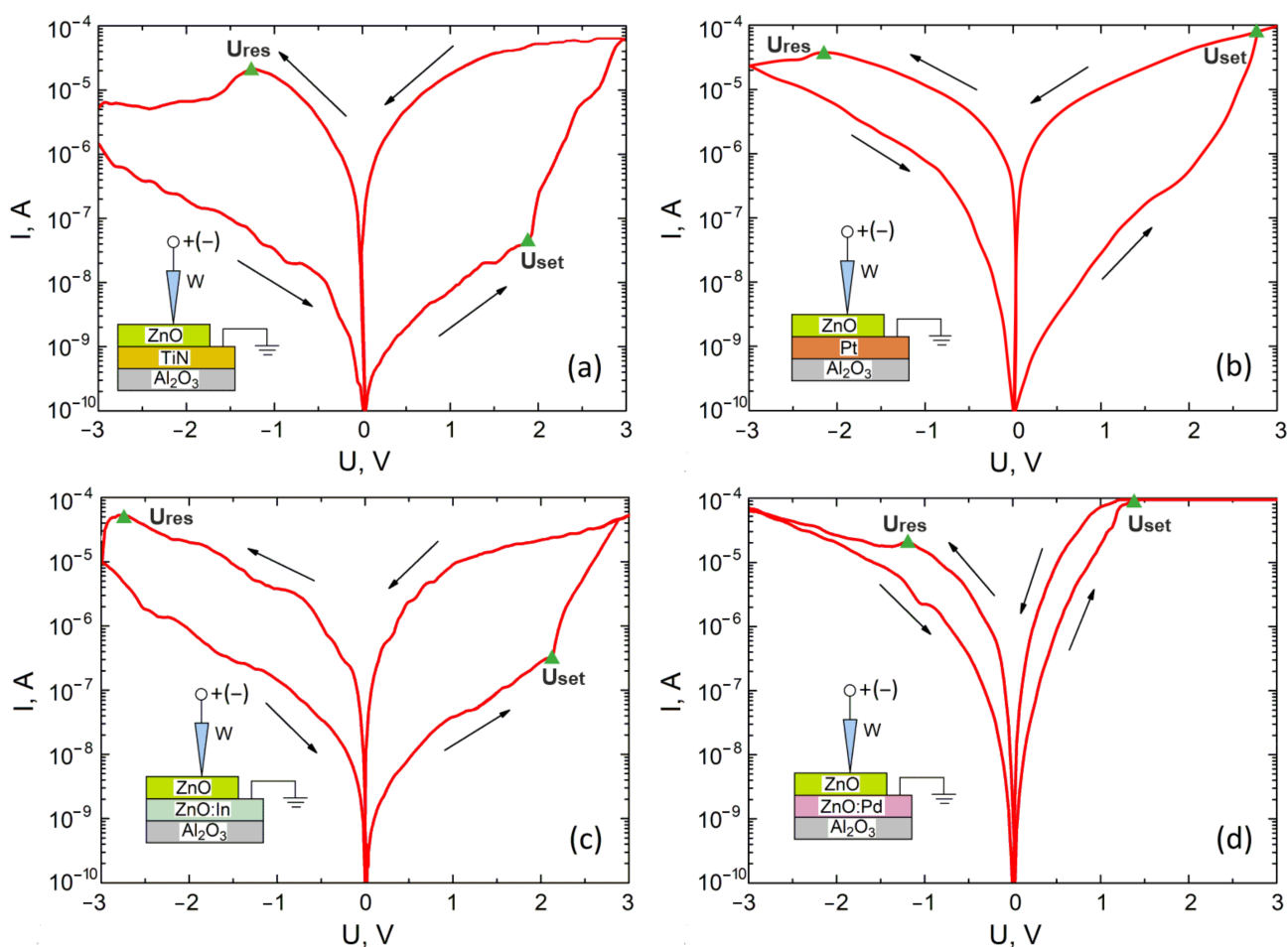


Figure 2. Current–voltage characteristics of the forming-free nanocrystalline ZnO films with various bottom-electrode materials: (a)—TiN; (b)—Pt; (c)—ZnO:In; (d)—ZnO:Pd.

Table 1. Resistive-switching parameters of the forming-free nanocrystalline ZnO films for different bottom-electrode materials.

Bottom-Electrode Material	TiN	Pt	ZnO:In	ZnO:Pd
R_{HRS} , M Ω	276.11 \pm 8.43	1141.37 \pm 13.24	61.38 \pm 2.54	0.67 \pm 0.01
R_{LRS} , M Ω	0.120 \pm 0.005	1.310 \pm 0.003	0.231 \pm 0.032	0.041 \pm 0.002
R_{HRS}/R_{LRS}	2307.8 \pm 166.4	871.3 \pm 12.1	272.5 \pm 48.7	16.4 \pm 1.1
U_{set} , V	1.9 \pm 0.2	2.7 \pm 0.4	2.3 \pm 0.2	1.2 \pm 0.1
U_{res} , V	−1.3 \pm 0.5	−2.2 \pm 0.6	−2.7 \pm 0.3	−1.3 \pm 0.1

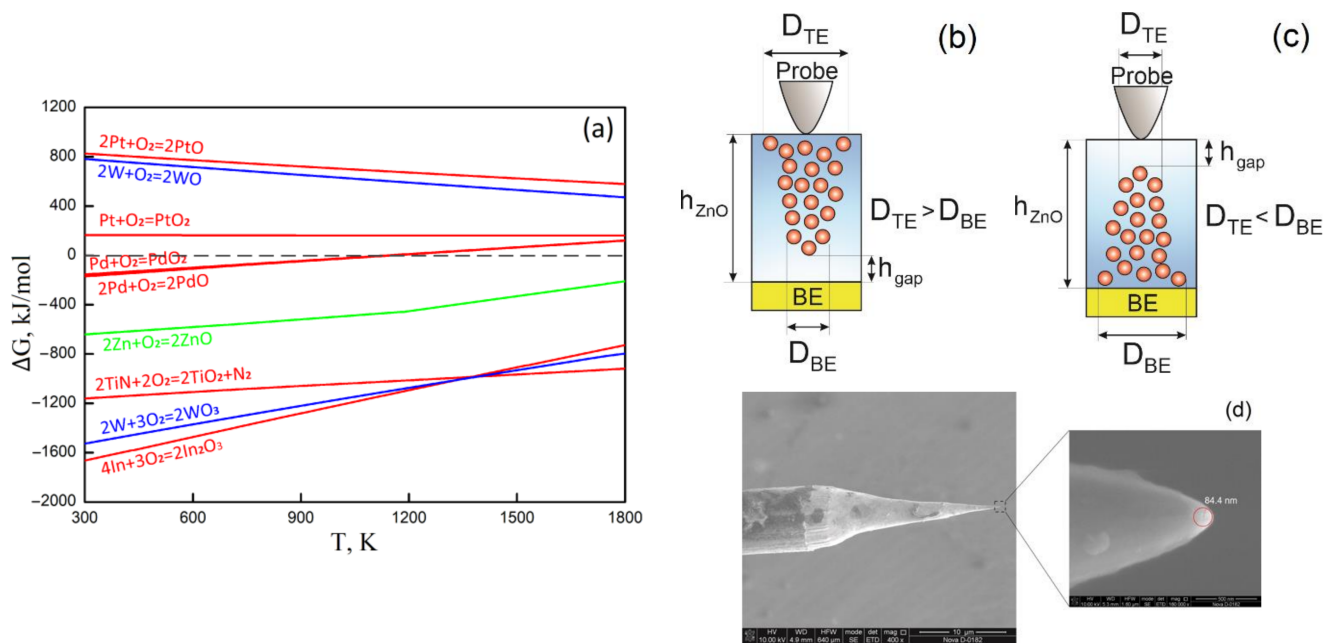


Figure 3. Electrode/oxide boundary influence on the resistive switching in the nanocrystalline ZnO film: (a)—Ellingham diagram; (b,c)—BE/ZnO/W structure scheme of resistive switching in the vicinity of the top electrode (b) and bottom electrode (c); (d)—SEM image of the top W electrode.

Analysis of the Ellingham diagram showed that the ΔG curve for $ZnO + O_2$ is higher than the ΔG curve for $TiN + O_2$ and $W + O_2$ (Figure 3a). This means that both the TiN/ZnO and ZnO/W interfaces are sources of oxygen vacancies. At the same time, because the ΔG curve for $TiN + O_2$ is higher than $W + O_2$ (Equation (S7)), it can be assumed that more oxygen vacancies are concentrated at the ZnO/W interface than at TiN/ZnO , that is, the base diameter is greater than the diameter of the apex of the nanoscale conduction channel ($D_{TE} > D_{BE}$) (Figure 3b). The reaction that results in the formation of oxide WO_3 (Equation (S8)) does not proceed, since its curve $\Delta G > 0$ kJ/mol. Therefore, it can be assumed that, with high probability, the generation and recombination of oxygen vacancies in the $TiN/ZnO/W$ structure, i.e., resistive switching, occurs at the TiN/ZnO interface (Figure 3b). Both ΔG curves for $Pt + O_2$ (Equations (S2) and (S3)) are located above 0 kJ/mol, which in theory implies the absence of a reduction reaction with the formation of oxygen vacancies at the Pt/ZnO interface. Therefore, with a high probability in the $Pt/ZnO/W$ structure, $D_{TE} > D_{BE}$ and resistive switching occurs at the Pt/ZnO interface (Figure 3b).

The ΔG curve for $In + O_2$ (Equation (S4)) is located lower than for $W + O_2$ and $Zn + O_2$; however, taking into account the fact that it is a doping component and that the number of its atoms is clearly less than the number of W atoms, as well as the fact that ΔG for $In + O_2$ and $W + O_2$ (Equation (S7)) are approximately the same, then resistive switching in the $ZnO:In/ZnO/W$ structure can occur both at the $ZnO:In/ZnO$ interface (Figure 3b) and at the ZnO/W interface (Figure 3c). To minimize the probability of the generation of two or more nanoscale conduction channels, we used a tungsten probe with a tip radius of 84.4 nm (Figure 3d).

The ΔG curves for $Pd + O_2$ (Equations (S5) and (S6)) are located near 0 kJ/mol, significantly higher than the ΔG curve for $W + O_2$ (Equation (S7)). Taking into account the fact that Pd is a dopant and the number of Pd atoms is clearly less than the number of W atoms, as well as the fact that the ΔG values for $W + O_2$ are positive at temperatures above 1138 K (Figure 3a), then, with high probability, we can assume that resistive switching occurs at the $ZnO:Pd/ZnO/W$ structure at the $ZnO:Pd/ZnO$ interface (Figure 3c).

Analysis of the Ellingham diagram showed that the ΔG curve for TiN + O₂ is lower than for Pt + O₂. Thus, we can assume that the number of oxygen vacancies at the TiN/ZnO interface is higher than at Pt/ZnO, that is, $D_{BE}(\text{TiN}) > D_{BE}(\text{Pt})$. This leads to the fact that the TiN/ZnO/W structure shows higher currents than the Pt/ZnO/W structure (Figure 2a,b) and hence lower resistance values R_{HRS} and R_{LRS} (Table 1).

The resistance R_{HRS} for the ZnO:In/ZnO/W structure is lower than that for TiN/ZnO/W, which can be explained by the fact that the destroyed section of the conduction channel h_{gap} for ZnO:In is smaller than that for TiN. In turn, the R_{LRS} for the ZnO:In/ZnO/W structure is larger than that for TiN/ZnO/W, which can be explained by the fact that the diameter of the apex of the nanoscale conduction channel (D_{BE}), due to the smaller number of In atoms compared to TiN, for ZnO:In is less than that for TiN. The large dispersion of the R_{HRS} and R_{LRS} of the ZnO:In/ZnO/W structure can be explained by the fact that resistive switching can occur with approximately the same probability at the ZnO:In/ZnO interface and ZnO/W (Figure 3c,d).

Resistance R_{HRS} and R_{LRS} for the ZnO:Pd/ZnO/W structure is significantly lower than for the other samples, despite the ΔG curves for Pd + O₂ (Equations (S4) and (S6)) lying above the ΔG curve for Zn + O₂ (Equation (S9)). It can be assumed that the current through the ZnO:Pd/ZnO interface is not associated with oxygen vacancies but with a rather low height of the potential barrier, because the difference between the work functions (ΔA) for Pd and ZnO is 4.98 eV and 5.20 eV ($\Delta A = 0.22$ eV). For comparison, the ΔA for In and ZnO was approximately 1.6 eV. A small dispersion of U_{set} and U_{res} was observed for samples with ZnO:In and ZnO:Pd, possibly because the bottom electrode and the ZnO film in these cases have the same values of the lattice constant, which affects the stability of the resistive switching parameters. Different values of the R_{HRS}/R_{LRS} ratio for all samples can be explained by different values of h_{gap} [14,15,23]. From this it follows that $h_{gap}(\text{TiN}) > h_{gap}(\text{Pt}) > h_{gap}(\text{ZnO:In}) > h_{gap}(\text{ZnO:Pd})$.

Analysis of the experimental results obtained from the nanoscale resistive switching study showed that the current flows mainly along the grain boundaries and represents localized light dots in the CAFM (Figure 4a). Thus, we assumed that the nanoscale conduction channels of oxygen vacancies are located along the boundary of the grains. To confirm our assumption, we formed the HRS spot $1 \times 1 \mu\text{m}^2$ on the ZnO surface, and then inside it, at the grain boundary, we formed the LRS spot about 22 nm diameter (Figure 4b). An increase in time from 60 to 10^4 s was shown to lead to an increase in resistance from $252.38 \pm 18.12 \text{ M}\Omega$ to $286.21 \pm 23.87 \text{ M}\Omega$ for HRS and from $5.16 \pm 0.43 \text{ M}\Omega$ to $6.17 \pm 0.62 \text{ M}\Omega$ for LRS (Figure 4c). The result obtained can be explained by the additional oxidation of the zinc oxide with atmospheric oxygen.

Thus, based on the obtained experimental results, it can be assumed that in our case the most suitable bottom-electrode material for forming-free nanocrystalline ZnO films is TiN. This conclusion is due to the TiN/ZnO sample having the highest R_{HRS}/R_{LRS} ratio, a parameter that determines the degree of multibit and hence the depth of learning of the future neuromorphic system. The structure of TiN/ZnO/W also showed acceptable values of $U_{set} = 1.9 \pm 0.2 \text{ V}$ and $U_{res} = -1.3 \pm 0.5 \text{ V}$, which is important for creating energy-efficient elements of memristive neuromorphic systems. It should also be noted that titanium nitride and platinum are among the materials most used for RRAM prototyping, as they have a large difference in work function with ZnO (ZnO/TiN ≈ 1.53 eV, ZnO/Pt 0.85 eV), which is important to ensure a high R_{HRS}/R_{LRS} ratio [68–70].

Analysis of the obtained experimental results showed that an increase in the number of laser pulses from 1000 to 5000 leads to an increase in the thickness of the nanocrystalline ZnO film from $7.2 \pm 2.5 \text{ nm}$ to $53.6 \pm 18.3 \text{ nm}$ and the surface roughness from $2.3 \pm 0.2 \text{ nm}$ to $16.2 \pm 2.1 \text{ nm}$ (Table 2). The slowdown in the film growth rate can be explained by different growth kinetics with an increase in the number of laser pulses: in the range from 1000 to 3000 laser pulses—film growth occurs due to the diffusion of atoms along the grain boundaries (ripening and surface mobility)—and in the range from 3000 to 5000 pulses, with transition to the usual kinetics of grain growth. The increase in roughness can be

explained by the intensification of the coalescence process with an increase in the thickness of the ZnO film. [71].

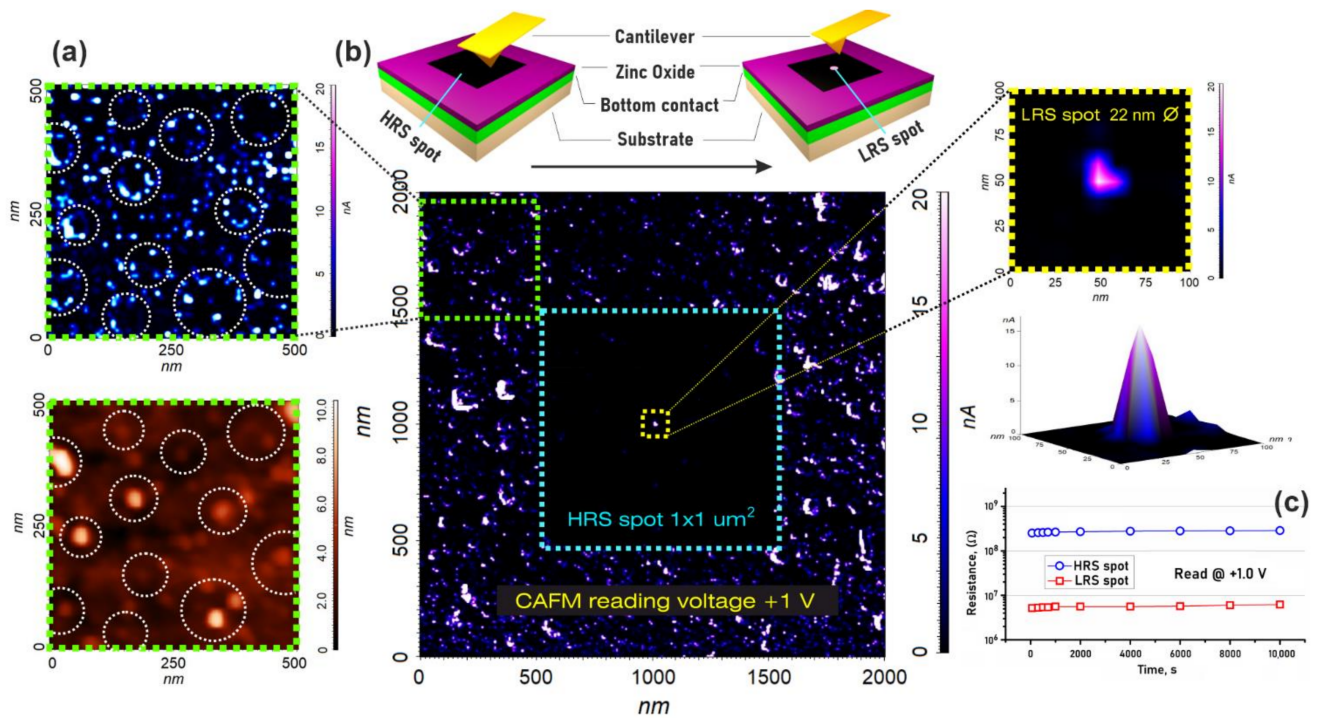


Figure 4. Conductive atomic-force microscopy of $\text{Al}_2\text{O}_3/\text{TiN}/\text{ZnO}$ structure: (a)—study of the impact of morphology on the ZnO film conductivity; (b)—scheme and experimental results of the ZnO film switching between HRS and LRS; (c)—retention test.

Table 2. PLD regime, experimental film thickness, and surface roughness of the forming-free nanocrystalline ZnO.

No. Sample	1	2	3	4	5
Substrate temperature, °C			500		
Number of laser pulses	1000	2000	3000	4000	5000
Laser pulse repetition rate, Hz			10		
Oxygen pressure, mTorr			0.5		
Film thickness (h_{ZnO}), nm	7.2 ± 2.5	23.6 ± 6.7	41.2 ± 9.7	48.8 ± 15.0	53.6 ± 18.3
Surface roughness (R_a), nm	2.3 ± 0.2	5.5 ± 1.2	8.1 ± 1.6	13.1 ± 1.9	16.2 ± 2.1

An analysis of the results obtained to study the effect of the thickness of the nanocrystalline ZnO film on its electrophysical parameters showed that an increase in h_{ZnO} from 7.2 ± 2.5 nm to 53.6 ± 18.3 nm led to an increase in electron concentration from $(1.8 \pm 0.3) \times 10^{19} \text{ cm}^{-3}$ to $(5.7 \pm 0.5) \times 10^{19} \text{ cm}^{-3}$ (Figure 5a), the electron mobility from $17.2 \pm 1.2 \text{ cm}^2/(\text{V}\cdot\text{s})$ to $1.9 \pm 0.5 \text{ cm}^2/(\text{V}\cdot\text{s})$ (Figure 5a), as well as an increase in resistivity from $(0.31 \pm 0.03) \times 10^{-2} \Omega\cdot\text{cm}$ to $(0.83 \pm 0.04) \times 10^{-2} \Omega\cdot\text{cm}$ (Figure 5b). This result can be explained by the fact that both bulk conductivity and grain-boundary conductivity contribute to the total conductivity of these films. In this case, with an increase in the film thickness (as well as an increase in the grain diameter), the contribution of the current flowing through the grain volume decreases because of an increase in the distance that charge carriers must overcome from one edge of the grain boundary to its other edge [72].

Analysis of experimental dependences showed that an increase in the thickness of the nanocrystalline ZnO film from 7.2 ± 2.5 nm to 53.6 ± 18.3 nm led to an increase in R_{HRS} from $8.12 \pm 0.79 \text{ M}\Omega$ to $386.71 \pm 18.22 \text{ M}\Omega$ and R_{LRS} from $0.030 \pm 0.007 \text{ M}\Omega$ to $0.182 \pm 0.018 \text{ M}\Omega$, respectively (Figure 6a). In this case, the $R_{\text{HRS}}/R_{\text{LRS}}$ ratio increased from 292.7 ± 94.6 to 2307.8 ± 166.4 with an increase in film thickness from 7.2 ± 2.5 nm to

41.2 ± 9.7 nm and decreased from 2307.8 ± 166.4 to 2154.7 ± 313.3 with an increase in film thickness from 41.2 ± 9.7 nm to 53.6 ± 18.3 nm (Figure 6b). One of the probable reasons for the increase in resistance of R_{HRS} is an increase in the length of the nanoscale conduction channel gap (h_{gap}) with an increase in the thickness of the forming-free nanocrystalline ZnO film, which is correlated with [73–75].

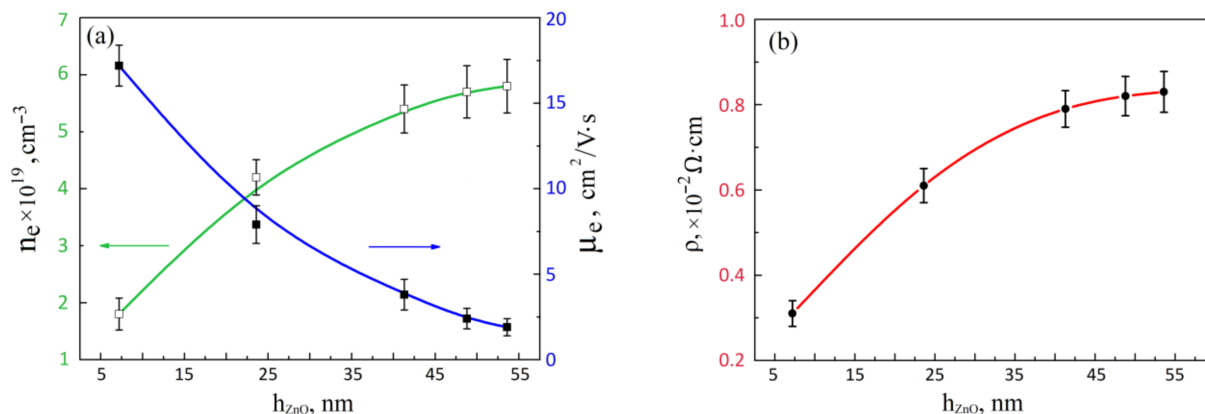


Figure 5. Experimental investigation of the thickness of the nanocrystalline ZnO film on electron concentration, electron mobility (a), and resistivity (b).

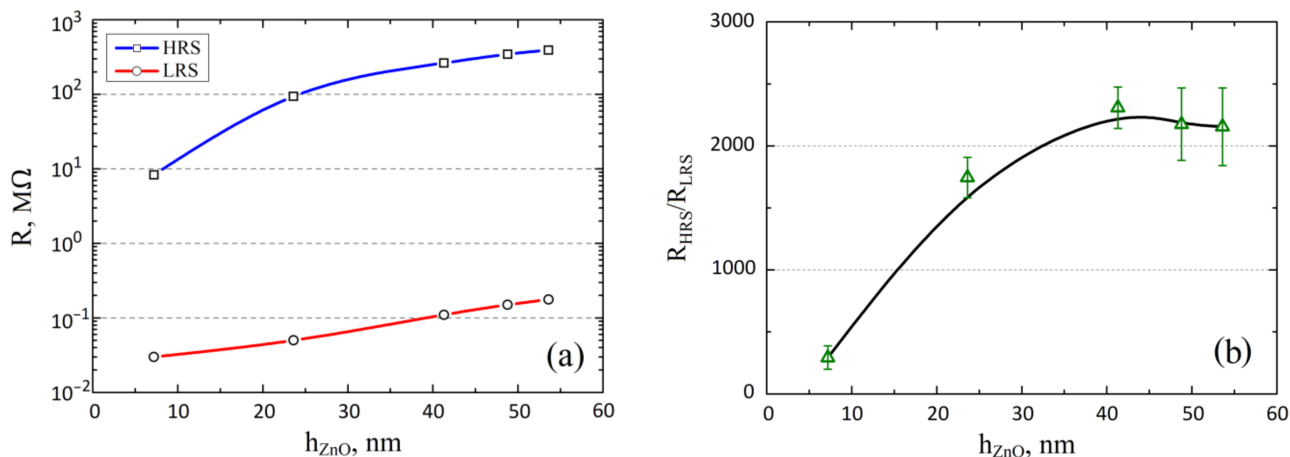


Figure 6. Dependence of the resistive switching parameters of the $\text{Al}_2\text{O}_3/\text{TiN}/\text{ZnO}/\text{W}$ structure on the thickness of the ZnO film: (a)— R_{HRS} and R_{LRS} ; (b)— $R_{\text{HRS}}/R_{\text{LRS}}$.

An increase in resistance R_{LRS} can be explained by a decrease in the diameter of the apex of the nanoscale conduction channel D_{BE} (Figure 3c) with an increase in the thickness of the nanocrystalline ZnO film. If we follow this hypothesis, then the decrease in $R_{\text{HRS}}/R_{\text{LRS}}$ can be explained by the fact that the $D_{\text{BE}}/h_{\text{gap}}$ ratio for films with a thickness from 7.2 ± 2.5 nm to 41.2 ± 9.7 nm is greater than for films with a thickness of 48.8 ± 15.0 nm and 53.6 ± 18.3 nm. The large dispersion of $R_{\text{HRS}}/R_{\text{LRS}}$ for films with a thickness of 48.8 ± 15.0 nm and 53.6 ± 18.3 nm can be explained by an increase in the nonuniformity of oxygen vacancy generation and recombination in most of the oxide film due to a decrease in the electron concentration with an increase in film thickness (Figure 5a), due to which the h_{gap} varies widely with each new switching cycle.

Analysis of the obtained experimental results obtained for the resistance values (Figure 7) (here, to avoid confusion, the resistances at one point on the surface of the ZnO film are designated $R_{\text{HRS}p}$ and $R_{\text{LRS}p}$ and at different points as $R_{\text{HRS}s}$ and $R_{\text{LRS}s}$) showed that an increase in the thickness of the film from 7.2 ± 2.5 nm to 53.6 ± 18.3 nm leads to an increase in the resistances $R_{\text{HRS}p}$ and $R_{\text{LRS}p}$ from $8.12 \pm 0.79 \text{M}\Omega$ to $386.71 \pm 18.22 \text{M}\Omega$ and from $0.030 \pm 0.007 \text{M}\Omega$ to $0.182 \pm 0.018 \text{M}\Omega$, respectively (Table 3). The resistances of $R_{\text{HRS}s}$

and R_{LRSs} increased from $7.93 \pm 0.93 \text{ M}\Omega$ to $378.81 \pm 38.82 \text{ M}\Omega$ and from $0.035 \pm 0.012 \text{ M}\Omega$ to $0.182 \pm 0.053 \text{ M}\Omega$, respectively. The R_{HRSsp}/R_{LRSsp} and R_{HRSs}/R_{LRSs} ratios increased from 292.7 ± 94.6 to 2154.7 ± 313.3 and from 267.1 ± 118.1 and 2342.1 ± 895.3 , respectively. The large dispersion of R_{HRS} and R_{LRS} values can be explained by the inhomogeneity of the morphology of nanocrystalline ZnO films (Figure 1), leading to an uneven concentration of oxygen vacancies in different areas of the nanocrystalline ZnO film.

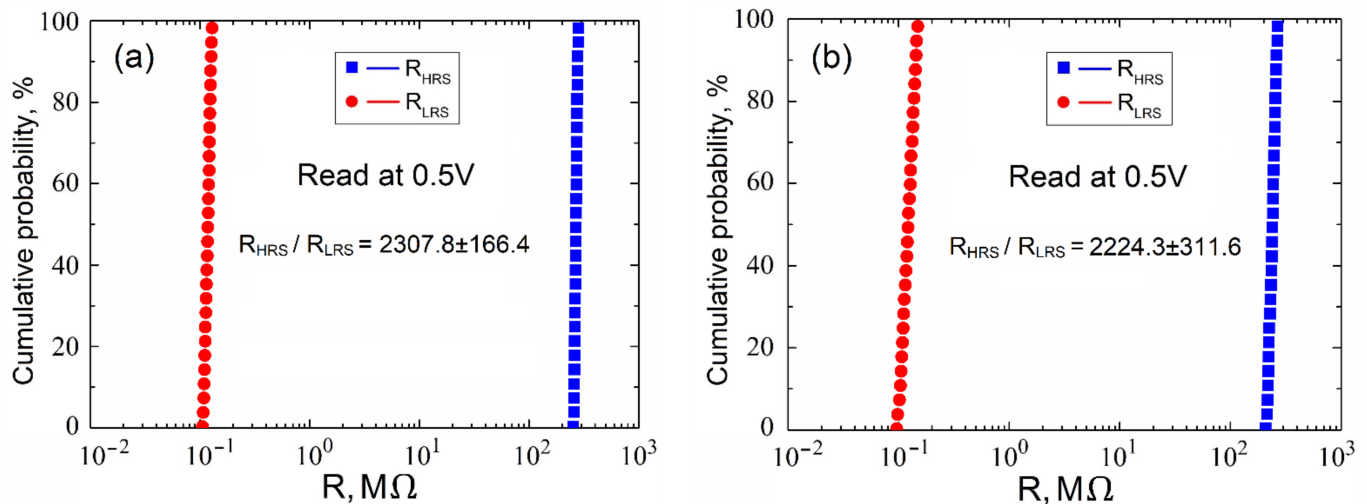


Figure 7. Investigation of resistive switching in the forming-free nanocrystalline ZnO film ($h_{\text{ZnO}} = 41.2 \pm 9.7 \text{ nm}$): (a)—at the same point on the film surface (endurance) and (b)—at different points on the film surface (homogeneity).

Table 3. Experimental investigations of the resistance of $\text{Al}_2\text{O}_3/\text{TiN}/\text{ZnO}/\text{W}$ at the same point (R_{HRSs} and R_{LRSs}) and at different points on the forming-free nanocrystalline ZnO film surface (R_{HRSsp} and R_{LRSsp}).

No. Sample	1	2	3	4	5
$R_{HRSsp}, \text{M}\Omega$	8.12 ± 0.79	104.22 ± 4.52	276.11 ± 8.43	305.12 ± 13.11	386.71 ± 18.22
$R_{LRSsp}, \text{M}\Omega$	0.030 ± 0.007	0.060 ± 0.003	0.120 ± 0.005	0.142 ± 0.013	0.182 ± 0.018
$R_{HRSs}, \text{M}\Omega$	7.93 ± 0.93	89.31 ± 12.7	250.54 ± 15.52	328.26 ± 39.41	378.81 ± 38.82
$R_{LRSs}, \text{M}\Omega$	0.035 ± 0.012	0.061 ± 0.002	0.114 ± 0.009	0.148 ± 0.026	0.182 ± 0.053
R_{HRSsp}/R_{LRSsp}	292.7 ± 94.6	1745.1 ± 162.6	2307.8 ± 166.4	2175.4 ± 291.4	2154.7 ± 313.3
R_{HRSs}/R_{LRSs}	267.1 ± 118.1	1472.5 ± 256.4	2224.3 ± 311.6	2336.8 ± 676.8	2342.1 ± 895.3

Therefore, for the fabrication of memristive elements of neuromorphic systems from the studied samples, the most preferable structure was $\text{TiN}/\text{ZnO}/\text{W}$ with the forming-free nanocrystalline ZnO thickness $41.2 \pm 9.7 \text{ nm}$, which has a sufficiently high ratio $R_{HRS}/R_{LRS} = 2307.8 \pm 166.4$ and has the best, compared to other samples, endurance and homogeneity.

Analysis of the results of the study of the influence of the top electrode on the effect of resistive switching in the structure $\text{Al}_2\text{O}_3/\text{TiN}/\text{ZnO}/\text{TiN}$ (Figure 8a,b) showed that the structure shows stable resistive switching with $U_{set} = 1.6 \pm 0.2 \text{ V}$ and $U_{res} = -0.8 \pm 0.3 \text{ V}$ (Figure 8c). The endurance test showed that R_{HRS} is $417.52 \pm 3.57 \text{ k}\Omega$ and R_{LRS} is $0.17 \pm 0.03 \text{ k}\Omega$ (Figure 8e). It was shown that the R_{HRS}/R_{LRS} ratio was about 2460 at a 0.5 V read voltage. A study of the device-to-device resistive switching showed that the R_{HRS}/R_{LRS} ratio was higher than two orders of magnitude (Figure 8d,f). Thus, the use of the top electrode made it possible to reduce the switching voltages U_{set} and U_{res} and to increase the R_{HRS}/R_{LRS} ratio. The results can be explained by the exclusion of atmospheric oxygen influence, which penetrates the ZnO film during resistive switching and creates additional energy barriers in the $\text{Al}_2\text{O}_3/\text{TiN}/\text{ZnO}$ structure.

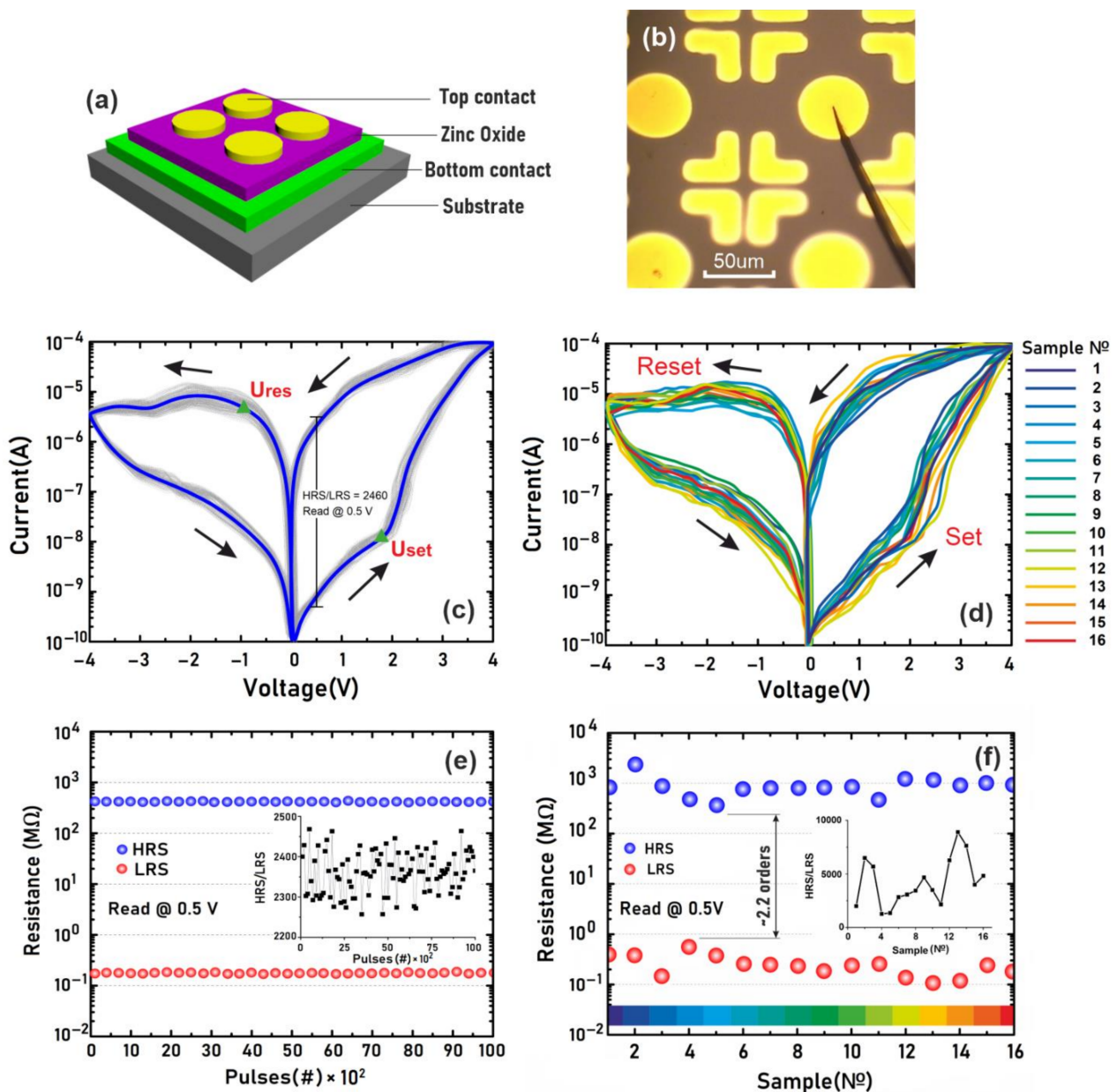


Figure 8. Investigation of resistive switching in the $\text{Al}_2\text{O}_3/\text{TiN}/\text{ZnO}/\text{TiN}$ memristive structures: (a)—conceptualization model; (b)—photomicrograph; (c)—current-voltage characteristics of a single device; (d)—current-voltage characteristics of 16 different devices; (e)—endurance test of a single device; (f)—reproducibility test.

It was shown that in the $\text{Al}_2\text{O}_3/\text{TiN}/\text{ZnO}/\text{TiN}$ memristive structure, an increase in U_A from 2 V to 7 V led to a decrease in the $R_{\text{HRS}}/R_{\text{LRS}}$ ratio from 2307.8 ± 166.4 to 1612.3 ± 112.4 (Figure 9a), and an increase in the t_A from 20 ms to 60 ms led to a decrease in the $R_{\text{HRS}}/R_{\text{LRS}}$ ratio from 2307.8 ± 166.4 to 1986.7 ± 126.8 (Figure 9b). The results can be explained by the increase in the concentration of oxygen vacancies and the nanoscale conducting channel diameters D_{TE} and D_{BE} (Figure 3b,c) in the nanocrystalline ZnO film with an increase in U_A and t_A .

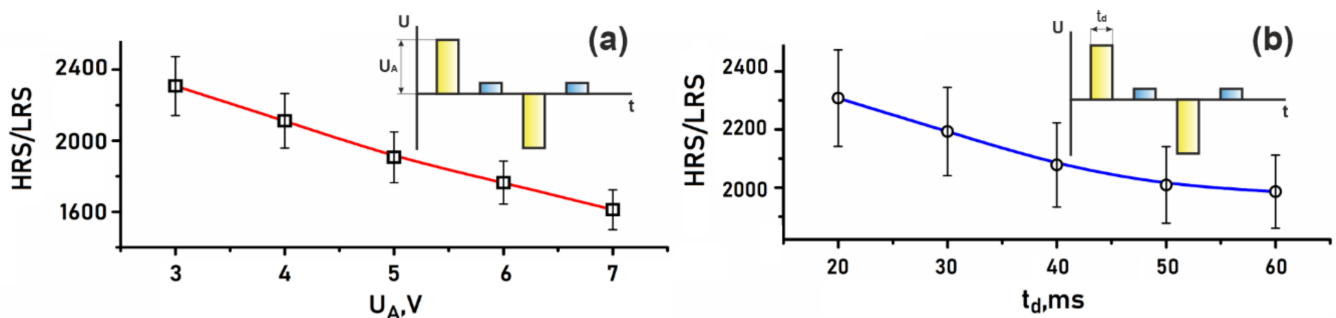


Figure 9. Experimental investigations of dependences of the RHRS/RLRS ratio on pulse: (a)—amplitude; (b)—duration.

4. Conclusions

The article presented the novel results of experimental studies of the bottom material and the impact of size on resistive switching in the nanocrystalline ZnO film fabricated by pulsed laser deposition. It was demonstrated that the nanocrystalline ZnO film exhibits a non-linear bipolar effect of forming-free resistive switching. The Ellingham diagrams for TiN + O₂, Pt + O₂, In + O₂, and Pd + O₂ were built. The sample with Pt showed the highest resistance values R_{HRS} and R_{LRS} and the highest value of $U_{set} = 2.7 \pm 0.4$ V. Samples with ZnO:In and ZnO:Pd bottom electrodes showed the lowest U_{set} and U_{res} values. It was shown that in our case, the most suitable bottom-electrode material for forming-free nanocrystalline ZnO films was TiN, since it had the highest R_{HRS}/R_{LRS} ratio, a parameter that determines the degree of multibit, and hence the depth of learning of the future neuromorphic system. Furthermore, the structure of TiN/ZnO/W demonstrates acceptable values of $U_{set} = 1.9 \pm 0.2$ V and $U_{res} = -1.3 \pm 0.5$ V, which is important to create energy-efficient elements of memristive neuromorphic systems.

It was shown that an increase in the number of laser pulses from 1000 to 5000 leads to an increase in the thickness of the nanocrystalline ZnO film and surface roughness. An analysis of electrophysical parameters showed that an increase in the thickness of the ZnO film from 7.2 ± 2.5 nm to 53.6 ± 18.3 nm leads to an increase in electron concentration from $(1.8 \pm 0.3) \times 10^{19}$ cm⁻³ to $(5.7 \pm 0.5) \times 10^{19}$ cm⁻³, a decrease in electron mobility from 17.2 ± 1.2 cm²/(V·s) to 1.9 ± 0.5 cm²/(V·s), and an increase in resistivity from $(0.31 \pm 0.03) \times 10^{-2}$ Ω·cm to $(0.83 \pm 0.04) \times 10^{-2}$ Ω·cm.

It was shown by the method CAFM that the in nanocrystalline ZnO films' current flows mainly along the grain boundaries and that the nanoscale conduction channels are located along the boundary of the grains.

The obtained experimental results showed that an increase in the thickness of the nanocrystalline ZnO film from 7.2 ± 2.5 nm to 41.2 ± 9.7 nm leads to an increase in the R_{HRS}/R_{LRS} ratio and decreases the R_{HRS}/R_{LRS} ratio with an increase in film thickness from 41.2 ± 9.7 nm to 53.6 ± 18.3 nm. Analysis of the results obtained for the endurance and the homogeneity tests showed that the ratios of R_{HRSp}/R_{LRSp} and R_{HRSs}/R_{LRSs} increased from 292.7 ± 94.6 to 2154.7 ± 313.3 and from 267.1 ± 118.1 and 2342.1 ± 895.3 , respectively. The large dispersion of the values of R_{HRSs} and R_{LRSs} can be explained by the inhomogeneity of the morphology of the nanocrystalline ZnO films, which leads to an uneven concentration of oxygen vacancies over the surface.

Therefore, it was shown that among the samples considered in this work, the TiN/ZnO/W structure with the forming-free nanocrystalline ZnO thickness 41.2 ± 9.7 nm is preferable for the manufacture of memristive neuromorphic systems due to the highest values of the R_{HRS}/R_{LRS} ratio and the relatively low values of U_{set} and U_{res} . It was shown that the use of the top electrode made it possible to reduce the switching voltages U_{set} and U_{res} and to increase the R_{HRS}/R_{LRS} ratio.

The results obtained can be used in the manufacturing of resistive-switching nanoscale devices for neuromorphic computing based on the forming-free nanocrystalline ZnO oxide films.

Supplementary Materials: The following are available online at <https://www.mdpi.com/article/10.3390/nano12030455/s1>, Figure S1: Experimental studies of the forming-free nanocrystalline ZnO film thickness: (a)—AFM-image; (b)—AFM cross section along the white line in (a); (c)—3D AFM-image; (d)—height histogram; Equations (S1)–(S9): Reduction reaction at the interface between the electrode and the forming-free nanocrystalline ZnO film.

Author Contributions: Conceptualization and validation, V.A.S.; methodology, V.A.S., R.V.T. and V.I.A.; investigation, R.V.T.; writing—original draft preparation, R.V.T. and V.A.S.; data curation and formal analysis, Z.E.V., A.V.S. and N.V.P.; visualization, R.V.T. and Z.E.V.; ZnO films growth Z.E.V.; supervision, V.A.S.; project administration, writing—review and editing, O.A.A. and V.A.S. All authors contributed to the writing of the manuscript, which was coordinated by V.A.S. All authors have read and agreed to the published version of the manuscript.

Funding: The reported study was funded by the Russian Foundation for Basic Research according to research project No. 19-29-03041_mk (Experimental studies of electrode material impact and nanoscale size effect on resistive switching in forming-free nanocrystalline ZnO films). The dependence of electrophysical parameters on the thickness of the forming-free nanocrystalline ZnO film was carried out with the financial support of the Russian Foundation for Basic Research, within the framework of project No. 19-38-60052. ZnO thin film samples' fabrication was carried out with the financial support of the by grant of the President of the Russian Federation № MK-6252.2021.4 and MK-767.2020.8. Investigation of the thickness of the forming-free nanocrystalline ZnO film and study of the morphology by the AFM method were carried out with the financial support of the Ministry of Science and Higher Education of the Russian Federation within the framework of a state task in the field of scientific activity No. 0852-2020-0015. Investigating resistive switching in the Al₂O₃/TiN/ZnO/TiN memristive structure was supported by a grant of the Russian Science Foundation No. 21-79-00216, <https://rscf.ru/project/21-79-00216/>, in Southern Federal University.

Conflicts of Interest: The authors declare no conflict of interest.

References

1. Schaller, R.R. Moore's law: Past, present and future. *IEEE Spectr.* **1997**, *34*, 52–59. [[CrossRef](#)]
2. Steinbuch, M.; Oomen, T.; Vermeulen, H. Motion Control, Mechatronics Design, and Moore's Law. *IEEJ J. Ind. Appl.* **2021**, *1*, 21006010. [[CrossRef](#)]
3. Burg, D.; Ausubel, J.H. Moore's Law revisited through Intel chip density. *PLoS ONE* **2021**, *16*, e0256245. [[CrossRef](#)] [[PubMed](#)]
4. Ajayan, J.; Nirmal, D.; Tayal, S.; Bhattacharya, S.; Arivazhagan, L.; Fletcher, A.A.; Ajitha, D. Nanosheet field effect transistors-A next generation device to keep Moore's law alive: An intensive study. *Microelectron. J.* **2021**, *114*, 105141. [[CrossRef](#)]
5. Xia, F.; Yang, L.T.; Wang, L.; Vinel, A. Internet of things. *Int. J. Commun. Syst.* **2012**, *25*, 1101. [[CrossRef](#)]
6. Xu, W.; Zhou, H.; Cheng, N.; Lyu, F.; Shi, W.; Chen, J.; Shen, X. Internet of vehicles in big data era. *IEEE/CAA J. Autom. Sin.* **2017**, *5*, 19–35. [[CrossRef](#)]
7. Radamson, H.H.; Zhu, H.; Wu, Z.; He, X.; Lin, H.; Liu, J.; Wang, G. State of the art and future perspectives in advanced CMOS technology. *Nanomaterials* **2020**, *10*, 1555. [[CrossRef](#)]
8. Smirnov, V. Nanolithography by local anodic oxidation of thin titanium film. In *Piezoelectrics and Nanomaterials: Fundamentals, Developments and Applications*, 1st ed.; Parinov, I., Ed.; Nanotechnology Science and Technology: Rostov-on-Don, Russia, 2015; Volume 1, pp. 85–103.
9. Tominov, R.V.; Vakulov, Z.E.; Avilov, V.I.; Khakhulin, D.A.; Polupanov, N.V.; Smirnov, V.A.; Ageev, O.A. The Effect of Growth Parameters on Electrophysical and Memristive Properties of Vanadium Oxide Thin Films. *Molecules* **2021**, *26*, 118. [[CrossRef](#)]
10. Klimin, V.S.; Tominov, R.V.; Avilov, V.I.; Dukhan, D.D.; Rezvan, A.A.; Zamburg, E.G.; Ageev, O.A. Nanoscale profiling and memristor effect of ZnO thin films for RRAM and neuromorphic devices application. *Int. Soc. Opt. Photonics* **2018**, *11022*, 110220E.
11. Smith, L.S. Neuromorphic systems: Past, present and future. *Brain Inspired Cogn. Syst.* **2008**, *1*, 167–182.
12. Zenke, F.; Bohtë, S.M.; Clopath, C.; Comşa, I.M.; Göltz, J.; Maass, W.; Masquelier, T.; Naud, R.; Neftci, E.O.; Petrovici, M.A.; et al. Visualizing a joint future of neuroscience and neuromorphic engineering. *Neuron* **2021**, *109*, 571–575. [[CrossRef](#)] [[PubMed](#)]
13. Demin, V.A.; Emelyanov, A.V.; Lapkin, D.A.; Erokhin, V.V.; Kashkarov, P.K.; Kovalchuk, M.V. Neuromorphic elements and systems as the basis for the physical implementation of artificial intelligence technologies. *Crystallogr. Rep.* **2016**, *61*, 992–1001. [[CrossRef](#)]

14. Ho, Y.; Huang, G.M.; Li, P. Nonvolatile memristor memory: Device characteristics and design implications. In Proceedings of the 2009 International Conference on Computer-Aided Design 2009, San Jose, CA, USA, 2–5 November 2009; Volume 1, pp. 485–490.
15. Chua, L. Resistance switching memories are memristors. *Appl. Phys. A* **2011**, *102*, 765–783. [[CrossRef](#)]
16. Yang, J.J.; Strukov, D.B.; Stewart, D.R. Memristive devices for computing. *Nat. Nanotechnol.* **2013**, *8*, 13. [[CrossRef](#)]
17. Ha, S.D.; Ramanathan, S. Adaptive oxide electronics: A review. *J. Appl. Phys.* **2011**, *110*, 14. [[CrossRef](#)]
18. Li, Y.; Wang, Z.; Midya, R.; Xia, Q.; Yang, J.J. Review of memristor devices in neuromorphic computing: Materials sciences and device challenges. *J. Phys. D Appl. Phys.* **2018**, *51*, 503002. [[CrossRef](#)]
19. Zhang, H.; Yoo, S.; Menzel, S.; Funck, C.; Cüppers, F.; Wouters, D.J.; Hoffmann-Eifert, S. Understanding the coexistence of two bipolar resistive switching modes with opposite polarity in Pt/TiO₂/Ti/Pt nanosized ReRAM devices. *ACS Appl. Mater. Interfaces* **2018**, *10*, 29766–29778. [[CrossRef](#)]
20. Bengel, C.; Cüppers, F.; Payvand, M.; Dittmann, R.; Waser, R.; Hoffmann-Eifert, S.; Menzel, S. Utilizing the Switching Stochasticity of HfO₂/TiO_x-Based ReRAM Devices and the Concept of Multiple Device Synapses for the Classification of Overlapping and Noisy Patterns. *Front. Neurosci.* **2021**, *15*, 661856. [[CrossRef](#)]
21. Chen, Y. ReRAM: History, status, and future. *IEEE Trans. Electron Devices* **2020**, *67*, 1420–1433. [[CrossRef](#)]
22. Li, B.; Doppa, J.R.; Pande, P.P.; Chakrabarty, K.; Qiu, J.X.; Li, H. 3D-ReG: A 3D ReRAM-based heterogeneous architecture for training deep neural networks. *ACM J. Emerg. Technol. Comput. Syst. (JETC)* **2020**, *16*, 1–24. [[CrossRef](#)]
23. Patil, V.L.; Patil, A.A.; Patil, S.V.; Khairnar, N.A.; Tarwal, N.L.; Vanalakar, S.A.; Dongale, T.D. Bipolar resistive switching, synaptic plasticity and non-volatile memory effects in the solution-processed zinc oxide thin film. *Mater. Sci. Semicond. Processing* **2020**, *106*, 104769. [[CrossRef](#)]
24. Partzsch, J.; Schuffny, R. Analyzing the scaling of connectivity in neuromorphic hardware and in models of neural networks. *IEEE Trans. Neural Netw.* **2011**, *22*, 919–935. [[CrossRef](#)] [[PubMed](#)]
25. Ventra, D.M.; Pershin, Y.V. Biologically-inspired electronics with memory circuit elements. *Adv. Neuromorphic Memristor Sci. Appl.* **2012**, *1*, 15–36.
26. Wang, H.; Li, H.; Pino, R.E. Memristor-based synapse design and training scheme for neuromorphic computing architecture. *Int. Jt. Conf. Neural Netw. (IJCNN)* **2012**, *1*, 1–5.
27. Dowling, V.J.; Slipko, V.A.; Pershin, Y.V. Probabilistic memristive networks: Application of a master equation to networks of binary ReRAM cells. *Chaos Solitons Fractals* **2021**, *142*, 110385. [[CrossRef](#)]
28. Al Chawa, M.M.; Picos, R.; Tetzlaff, R. A Compact Memristor Model for Neuromorphic ReRAM Devices in Flux-Charge Space. *IEEE Trans. Circuits Syst. I Regul. Pap.* **2021**, *68*, 3631–3641. [[CrossRef](#)]
29. Xiao, Z.; Huang, J. Energy-efficient hybrid perovskite memristors and synaptic devices. *Adv. Electron. Mater.* **2016**, *2*, 1600100. [[CrossRef](#)]
30. Chua, L. Memristor—the missing circuit element. *IEEE Trans. Circuit Theory* **1971**, *18*, 507–519. [[CrossRef](#)]
31. Azghadi, M.R.; Linares-Barranco, B.; Abbott, D.; Leong, P.H. A hybrid CMOS-memristor neuromorphic synapse. *IEEE Trans. Biomed. Circuits Syst.* **2016**, *11*, 434–445. [[CrossRef](#)]
32. Saxena, V. A compact CMOS memristor emulator circuit and its applications. In Proceedings of the 2018 IEEE 61st International Midwest Symposium on Circuits and Systems (MWSCAS), Windsor, ON, Canada, 5–8 August 2018; Volume 1, pp. 190–193.
33. Lin, J.; Yuan, J.S. A scalable and reconfigurable in-memory architecture for ternary deep spiking neural network with ReRAM based neurons. *Neurocomputing* **2020**, *375*, 102–112. [[CrossRef](#)]
34. Vishwakarma, K.; Kishore, R.; Datta, A. Symmetric Linear Rise and Fall of Conductance in a Trilayer Stack Engineered ReRAM-Based Synapse. *ACS Appl. Electron. Mater.* **2020**, *2*, 3263–3269. [[CrossRef](#)]
35. Gale, E. TiO₂-based memristors and ReRAM: Materials, mechanisms and models (a review). *Semicond. Sci. Technol.* **2014**, *9*, 104004. [[CrossRef](#)]
36. Al-Mamun, M.; Orłowski, M. Electric conductivity of remotely heated Cu nanofilaments in Cu/TaO_x/Pt ReRAM cells. *J. Appl. Phys.* **2020**, *129*, 055107. [[CrossRef](#)]
37. Li, Y.; Zhong, Y.; Xu, L.; Zhang, J.; Xu, X.; Sun, H.; Miao, X. Ultrafast synaptic events in a chalcogenide memristor. *Sci. Rep.* **2013**, *3*, 1–7. [[CrossRef](#)] [[PubMed](#)]
38. Qian, W.H.; Cheng, X.F.; Zhou, J.; He, J.H.; Li, H.; Xu, Q.F.; Lu, J.M. Lead-free perovskite MASnBr₃-based memristor for quaternary information storage. *InfoMat* **2020**, *2*, 743–751. [[CrossRef](#)]
39. Romero, F.J.; Toral-Lopez, A.; Ohata, A.; Morales, D.P.; Ruiz, F.G.; Godoy, A.; Rodriguez, N. Laser-Fabricated reduced graphene oxide memristors. *Nanomaterials* **2019**, *9*, 897. [[CrossRef](#)]
40. Mittermeier, B.; Bednar, A.; Kaiser, M.; Ruediger, A.; Schindler, C. Comparison of spin-on-glass and WO₃ as an insulating layer for printed resistive memory devices. *Mater. Technol.* **2019**, *34*, 350–355. [[CrossRef](#)]
41. Cao, X.; Li, X.; Gao, X.; Yu, W.; Liu, X.; Zhang, Y.; Cheng, X. Forming-free colossal resistive switching effect in rare-earth-oxide Gd₂O₃ films for memristor applications. *J. Appl. Phys.* **2009**, *106*, 073723. [[CrossRef](#)]
42. Li, Y.; Chu, J.; Duan, W.; Cai, G.; Fan, X.; Wang, X.; Pei, Y. Analog and digital bipolar resistive switching in solution-combustion-processed NiO memristor. *ACS Appl. Mater. Interfaces* **2018**, *10*, 24598–24606. [[CrossRef](#)]
43. Awais, M.N.; Muhammad, N.M.; Navaneethan, D.; Kim, H.C.; Jo, J.; Choi, K.H. Fabrication of ZrO₂ layer through electrohydrodynamic atomization for the printed resistive switch (memristor). *Microelectron. Eng.* **2013**, *103*, 167–172. [[CrossRef](#)]

44. Dongale, T.D.; Mohite, S.V.; Bagade, A.A.; Gaikwad, P.K.; Patil, P.S.; Kamat, R.K.; Rajpure, K.Y. Development of Ag/WO₃/ITO thin film memristor using spray pyrolysis method. *Electron. Mater. Lett.* **2015**, *11*, 944–948. [[CrossRef](#)]
45. Wang, X.; Qian, H.; Guan, L.; Wang, W.; Xing, B.; Yan, X.; Wang, Y. Influence of metal electrode on the performance of ZnO based resistance switching memories. *J. Appl. Phys.* **2017**, *122*, 154301. [[CrossRef](#)]
46. She, Y.; Peng, Y.; Tang, B.; Hu, W.; Qiu, J.; Tang, X.; Bao, D. Bipolar resistive switching effects with self-compliance and multilevel storage characteristics in Ag/MgZnO/Si structures. *Ceram. Int.* **2018**, *44*, S11–S14. [[CrossRef](#)]
47. Shan, F.; Guo, H.B.; Kim, H.S.; Lee, J.Y.; Sun, H.Z.; Gon Choi, S.; Kim, S.J. Enhanced electrical performance of structurally engineered memristor devices with multi-stacked indium zinc oxide films. *Phys. Status Solidi (A)* **2020**, *217*, 1900967. [[CrossRef](#)]
48. Mika, K.; Socha, R.P.; Nyga, P.; Wiercigroch, E.; Małek, K.; Jarosz, M.; Zaraska, L. Electrochemical synthesis and characterization of dark nanoporous zinc oxide films. *Electrochim. Acta* **2019**, *305*, 349–359. [[CrossRef](#)]
49. Dang, B.; Wu, Q.; Song, F.; Sun, J.; Yang, M.; Ma, X.; Hao, Y. A bio-inspired physically transient/biodegradable synapse for security neuromorphic computing based on memristors. *Nanoscale* **2018**, *10*, 20089–20095. [[CrossRef](#)]
50. Tominov, R.V.; Smirnov, V.A.; Avilov, V.I.; Fedotov, A.A.; Klimin, V.S.; Chernenko, N.E. Formation of ZnO memristor structures by scratching probe nanolithography. *Mater. Sci. Eng.* **2018**, *443*, 012036. [[CrossRef](#)]
51. Bhati, V.S.; Ranwa, S.; Fanetti, M.; Valant, M.; Kumar, M. Efficient hydrogen sensor based on Ni-doped ZnO nanostructures by RF sputtering. *Sens. Actuators B Chem.* **2018**, *255*, 588–597. [[CrossRef](#)]
52. Tominov, R.V.; Zamburg, E.G.; Khakhulin, D.A.; Klimin, V.S.; Smirnov, V.A.; Chu, Y.H.; Ageev, O.A. Investigation of resistive switching of Zn_xTi_yHf_zO_i nanocomposite for RRAM elements manufacturing. *J. Phys. Conf. Ser.* **2017**, *917*, 032023. [[CrossRef](#)]
53. Zhao, X.; Li, Y.; Ai, C.; Wen, D. Resistive switching characteristics of Li-doped ZnO thin films based on magnetron sputtering. *Materials* **2019**, *12*, 1282. [[CrossRef](#)]
54. Li, S.S.; Su, Y.K. Oxygen-Vacancy Induced Resistive Switching Effect in Mn-Doped ZnO Memory Devices. *Phys. Status Solidi (RRL)—Rapid Res. Lett.* **2019**, *13*, 1800453. [[CrossRef](#)]
55. Li, S.S.; Su, Y.K. Improvement of the performance in Cr-doped ZnO memory devices via control of oxygen defects. *RSC Adv.* **2019**, *9*, 2941–2947. [[CrossRef](#)]
56. Boppidi, P.K.R.; Raj, P.M.P.; Challagulla, S.; Gollu, S.R.; Roy, S.; Banerjee, S.; Kundu, S. Unveiling the dual role of chemically synthesized copper doped zinc oxide for resistive switching applications. *J. Appl. Phys.* **2018**, *124*, 214901. [[CrossRef](#)]
57. Kao, M.C.; Chen, H.Z.; Chen, K.H.; Shi, J.B.; Weng, J.H.; Chen, K.P. Resistive switching behavior and optical properties of transparent Pr-doped ZnO based resistive random access memory. *Thin Solid Film.* **2020**, *697*, 137816. [[CrossRef](#)]
58. Abbas, H.; Abbas, Y.; Hassan, G.; Sokolov, A.S.; Jeon, Y.R.; Ku, B.; Choi, C. The coexistence of threshold and memory switching characteristics of ALD HfO₂ memristor synaptic arrays for energy-efficient neuromorphic computing. *Nanoscale* **2020**, *12*, 14120–14134. [[CrossRef](#)] [[PubMed](#)]
59. Porro, S.; Bejtka, K.; Jasmin, A.; Fontana, M.; Milano, G.; Chiolerio, A.; Ricciardi, C. A Multi-level memristor based on atomic layer deposition of iron oxide. *Nanotechnology* **2018**, *29*, 495201. [[CrossRef](#)]
60. Hadi, S.A.; Humood, K.M.; Abi Jaoude, M.; Abunahla, H.; Al Shehhi, H.F.; Mohammad, B. Bipolar Cu/HfO₂/p++ Si memristors by sol-gel spin coating method and their application to environmental sensing. *Sci. Rep.* **2019**, *9*, 1–15.
61. Santos, Y.P.; Valença, E.; Machado, R.; Macêdo, M.A. A novel structure ZnO-Fe-ZnO thin film memristor. *Mater. Sci. Semicond. Processing* **2018**, *86*, 43–48. [[CrossRef](#)]
62. Xue, Q.; Wang, Y.C.; Wei, X.H. Synaptic plasticity of room-temperature fabricated amorphous MoO_x film based memristor. *Appl. Surf. Sci.* **2019**, *479*, 469–474. [[CrossRef](#)]
63. Ageev, O.A.; Gusev, E.Y.; Zamburg, E.G.; Vakulov, D.E.; Vakulov, Z.E.; Shumov, A.V.; Ivonin, M.N. Nanocrystalline ZnO films grown by PLD for NO₂ and NH₃ sensor. *Appl. Mech. Mater.* **2014**, *475*, 446–450.
64. Tominov, R.V.; Vakulov, Z.E.; Avilov, V.I.; Khakhulin, D.A.; Fedotov, A.A.; Zamburg, E.G.; Smirnov, V.A.; Ageev, O.A. Synthesis and Memristor Effect of a Forming-Free ZnO Nanocrystalline Films. *Nanomaterials* **2020**, *10*, 1007. [[CrossRef](#)] [[PubMed](#)]
65. Smirnov, V.A.; Tominov, R.V.; Avilov, V.I.; Alyabieva, N.I.; Vakulov, Z.E.; Zamburg, E.G.; Ageev, O.A. Investigation into the Memristor Effect in Nanocrystalline ZnO Films. *Semiconductors* **2019**, *53*, 72–77. [[CrossRef](#)]
66. Chen, Y.L.; Ho, M.S.; Lee, W.J.; Chung, P.F.; Balraj, B.; Sivakumar, C. The mechanism underlying silicon oxide based resistive random-access memory (ReRAM). *Nanotechnology* **2020**, *31*, 145709. [[CrossRef](#)] [[PubMed](#)]
67. Yang, B.; Xu, N.; Li, C.; Huang, C.; Ma, D.; Liu, J.; Fang, L. A forming-free ReRAM cell with low operating voltage. *IEICE Electron. Express* **2020**, *17*, 20200343. [[CrossRef](#)]
68. Xu, N.; Liu, L.; Sun, X.; Liu, X.; Han, D.; Wang, Y.; Yu, B. Characteristics and mechanism of conduction/set process in TiN/ZnO/Pt resistance switching random-access memories. *Appl. Phys. Lett.* **2008**, *92*, 232112. [[CrossRef](#)]
69. Yang, J.J.; Pickett, M.D.; Li, X.; Ohlberg, D.A.; Stewart, D.R.; Williams, R.S. Memristive switching mechanism for metal/oxide/metal nanodevices. *Nat. Nanotechnol.* **2008**, *3*, 429–433. [[CrossRef](#)]
70. Goux, L.; Czarnecki, P.; Chen, Y.Y.; Pantisano, L.; Wang, X.; Degraeve, R.; Altimime, L. Evidences of oxygen-mediated resistive-switching mechanism in TiN/HfO₂/Pt cells. *Appl. Phys. Lett.* **2010**, *97*, 243509. [[CrossRef](#)]
71. Develos, K.D.; Kusunoki, M.; Mukaida, M.; Ohshima, S. Effect of deposition rate on the surface morphology of CeO₂ films deposited by pulsed laser deposition. *Phys. C Supercond.* **1999**, *320*, 21–30. [[CrossRef](#)]

72. Rupp, J.L.; Infortuna, A.; Gauckler, L.J. Microstrain and self-limited grain growth in nanocrystalline ceria ceramics. *Acta Mater.* **2006**, *54*, 1721–1730. [[CrossRef](#)]
73. Chiu, F.C. A review on conduction mechanisms in dielectric films. *Adv. Mater. Sci. Eng.* **2014**, *2014*, 1–18. [[CrossRef](#)]
74. Luo, J.M.; Lin, S.P.; Zheng, Y.; Wang, B. Nonpolar resistive switching in Mn-doped BiFeO₃ thin films by chemical solution deposition. *Appl. Phys. Lett.* **2012**, *101*, 062902. [[CrossRef](#)]
75. Das, O.P.; Pandey, S.K. Effect of conducting filament radius on local temperature and activation power of ON-state ReRAM device. *Semicond. Sci. Technol.* **2021**, *36*, 095039. [[CrossRef](#)]